Journal of
Materials Chemistry C

ROYAL SOCIETY
OF CHEMISTRY

PAPER

View Article Online
View Journal | View Issue

Check for updates

Cite this: *J. Mater. Chem. C*, 2023, **11**, 6730

Confinement of MACl guest in 2D ZIF-8 triggers interface and bulk passivation for efficient and UV-stable perovskite solar cells†

Zuoming Jin,[a] Bin Li,[b] Yutian Xu,[a] Boya Zhu,[a] Gaiqin Ding,[a] Yuanqiang Wang,[a] Jingxia Yang,[a] Qinghong Zhang[b] and Yichuan Rui*[a]

Received 17th February 2023,
Accepted 1st May 2023

DOI: 10.1039/d3tc00609c

rsc.li/materials-c

The rational passivation of the defects at the buried interface plays a significant role in reducing energy loss and improving the photovoltaic performance of perovskite solar cells (PSCs). Herein, we have applied a metal–organic framework (MOF)-based host–guest system consisting of zeolitic imidazolate framework-8 (ZIF-8) nanosheets confined with methylammonium chloride (MACl) to modify the SnO_2/perovskite interface. The MACl@ZIF-8 not only effectively reduces the oxygen vacancies on SnO_2, but also binds with the uncoordinated Pb^{2+} and halogen ions at the bottom of the perovskite layer. Moreover, the loaded MACl guest plays the role of both crystalline seeds involved in the formation of ZIF-8@perovskite heterojunctions and organic cation vacancy passivators. Thus, the simultaneous passivation of the buried interface and bulk phase of the perovskite is realized, and the photovoltaic performance of devices is enhanced considerably with an optimal efficiency of 22.10%. The introduction of MACl@ZIF-8 also allows the device to achieve excellent moisture stability due to better crystallinity and fewer phase defects. In particular, the UV shielding characteristic of the imidazole ligands in ZIF-8 results in a significant increase in the UV resistance capability.

1. Introduction

After only one decade of development, perovskite solar cells (PSCs) have already achieved a tremendous certified efficiency of 25.7%.[1] Yet, the power conversion efficiency (PCE) and long-term stability of the devices are still worthy of the efforts to meet the requirements for commercialization. To obtain a higher PCE that gets closer to the theoretical Shockley–Queisser limit efficiency (30.5%)[2] and better stability, many strategies have been used to passivate the defects present at the interfaces of the electron transport layer (ETL)/perovskite and perovskite/hole transport layer (HTL) and in the bulk phase of perovskites, including interfacial engineering,[3,4] additive engineering,[5,6] and solvent engineering.[7,8] Among them, it is significant and necessary for PSCs to reduce the trap density at the buried interface because the defect centers could lead to severe carrier accumulation and non-radiative recombination.[9,10] The defects on the surface of SnO_2 and at the bottom of perovskite seriously hamper device performance. More specifically, oxygen vacancies, hydroxyl groups, and unsaturated coordinated metal atoms commonly exist on the SnO_2 surface.[11,12] For the bottom surface of the perovskite, sub-micro-scale extended defects, contact-induced reconstruction and inhomogeneity of halide lead are regularly present.[13,14] These deep-level defects are very vulnerable and can induce interfacial reactions and open-circuit voltage loss by becoming non-radiative recombination centers.[15,16]

In the typical organic–inorganic halide perovskite, the thermally unstable MA^+ tends to partially evaporate and escape during the annealing process of the film. This could induce component stoichiometry imbalance and bulk phase defects.[17,18] Thus, many cation vacancies are left and result in the unfavorable transfer of photogenerated carriers. Therefore, cation vacancy compensation for MA-based perovskite becomes an effective way to enhance device performance.

Bimolecular or host–guest passivation systems have been explored to achieve dual passivation of the buried interface and the bulk phase simultaneously. Zhu *et al.* developed a depth-dependent manipulation strategy to modulate both the interface defects and bulk defects by two kinds of molecules. Since different sizes exhibit different permeabilities in the perovskite layer, the defects at different locations can be passivated.[19] Grätzel *et al.* also designed a host–guest method by employing dibenzo-21-crown-7 (DB21C7)-loaded Cs^+ to form a well-defined

---

[a] *College of Chemistry and Chemical Engineering, Shanghai University of Engineering Science, Shanghai 201620, P. R. China. E-mail: ryc713@126.com*
[b] *State Key Laboratory for Modification of Chemical Fibers and Polymer Materials, College of Materials Science and Engineering, Donghua University, Shanghai 201620, P. R. China*

† Electronic supplementary information (ESI) available. See DOI: https://doi.org/10.1039/d3tc00609c

host–guest complex, thus delivering Cs^+ ions into the interior while modulating the perovskite. This provides a local nanoscale doping gradient that supports photoinduced charge separation while passivating surface and bulk defects, stabilizing the perovskite phase through synergistic effects of the host, guest and host–guest complexes.[20] The defects at the buried interface and in the bulk phase are prone to inducing severe carrier recombination and both the PCE and long-term stability suffer from outside environmental factors, which result in poor photovoltaic performance. Therefore, a robust and functionalized modifier that meets multiple passivation requirements is essential.

Metal–organic frameworks (MOFs) are a class of crystalline inorganic–organic hybrid materials that have a wide range of special characteristics.[21] Their multimodal porosity and open architecture enable effective mass transmission. MOFs also exhibit outstanding chemical and physical stability, leading to a wide range of applications in biology,[22] sensing,[23] and catalysis.[24] There have been some explorations of MOFs in the field of PSCs. Nevertheless, these studies mainly focused on three-dimensional (3D) MOFs, which were used as scaffolds or modifiers.[25,26] The relatively large size and insulation, which are characteristic of 3D MOFs, impede their application in PSCs. As two-dimensional (2D) materials, 2D MOFs are a series of materials that possess regular porous structures with large specific surface area,[27] thus attracting much attention due to their excellent properties such as tunable structure, rich active sites, and outstanding physical and chemical stability.[28,29] In particular, 2D MOFs provide more exposed active sites than 3D MOFs, which enable them to be used to improve device performance more effectively.[30,31] Jen *et al.* reported a thiol-functionalized 2D conjugated MOF as an electron-extraction layer at the perovskite/cathode interface to capture the leaked Pb^{2+} from the degraded perovskite by forming water-insoluble solids; thus, excellent stability of devices was obtained and the harmful effect on the environment was suppressed.[32] Therefore, 2D MOFs have sufficient capabilities and unique advantages in the field of photovoltaics.

In this study, we synthesized 2D zeolitic imidazolate framework-8 (ZIF-8) nanosheets by a unique mixed solvent method and then embedded methylammonium chloride (MACl) into the framework. The as-obtained MACl@ZIF-8 was applied as a modifier to passivate the buried interface between SnO_2 and the perovskite layer, which realized excellent dual-defect passivation in both the buried interface and the bulk phase of the perovskite. With the reduced non-radiative recombination and enhanced electron transportation, the champion efficiency of the PSCs was boosted from 19.61% to 22.10%. In addition, the UV-resistant characteristics and crystallization-regulated roles of ZIF-8 empowered the devices with improved UV and humidity stability.

2. Results and discussion

Fig. 1(a) shows the synthetic process of MACl@ZIF-8. The framework of ZIF-8 is composed of the Zn ion as the node and 2-MIM as the backbone, and MACl seeds are confined into the pores of ZIF-8 by post-treatment, leading to a host–guest system. In this structure, the guest MACl seeds could produce hydrogen bonds with the ZIF-8 host. Specifically, the N atoms on the MACl had hydrogen-bond interactions with the N–H groups on the ZIF-8 framework.[33,34] Moreover, to synthesize 2D ZIF-8, a mixed solvent (DMF and ethanol) method was developed to obtain uniformly sized ZIF-8 nanosheets (Fig. 1(b)) because the DMF–ethanol (aprotic-protic mixed solvent) provides an isomeric 2D coordination system. The steric effect of DMF also impedes the aggregated growth of 2D products.[35] After the embedment of MACl, the morphology of MACl@ZIF-8 showed no obvious change (Fig. 1(c)), while the dynamic light scattering (DLS) results exhibited a smaller size distribution (Fig. 1(d)). It is possible that the intermolecular hydrogen interactions between MACl@ZIF-8 and DMF molecules in the form of $C{=}O\cdots H{-}N$ make a better dispersion.

XRD tests were performed to characterize the crystallinity and purity of the prepared ZIF-8 and MACl@ZIF-8. Fig. 1(e) shows the main diffraction peaks located at 7.3°, 10.4°, 12.7°, and 18.1°, corresponding to the (011), (002), (112), and (222) planes of ZIF-8. Both samples exhibited excellent crystallinity and the structure of ZIF-8 did not change much after loading MACl, which also proves the excellent structure stability of MACl@ZIF-8. The FTIR results in Fig. S1 (ESI†) also confirmed the high purity of ZIF-8 and MACl@ZIF-8,[36] and no significant changes in the FTIR peaks of the products were observed after loading MACl. To verify that MACl seeds successfully occupied the holes of ZIF-8, the specific surface areas of ZIF-8 and MACl@ZIF-8 were measured. As shown in Fig. 1(f), the specific surface area of MACl@ZIF-8 is 166.75 $m^2\ g^{-1}$, which is significantly lower than 1014.95 $m^2\ g^{-1}$ of pristine ZIF-8, indicating that most pores of ZIF-8 are occupied by MACl. The pore size distribution curves also confirmed the disappearance of the pores (Fig. 1(g)).

MACl@ZIF-8 was redispersed in DMF and spin-coated on the SnO_2 ETLs. Fig. 2(a) and (b) demonstrate the surface SEM images of SnO_2 films without and with MACl@ZIF-8. Both films exhibited compact and pinhole-free morphologies. Notably, the MACl@ZIF-8-modified SnO_2 film is more uniform and smoother. To determine the uniformity of MACl@ZIF-8 on SnO_2, we used EDS to analyze the distribution of the elements. As shown in Fig. 2(c), the EDS mappings of Zn, N, and Cl further identified the uniform distribution of MACl@ZIF-8 on SnO_2. The cross-sectional SEM image of MACl@ZIF-8-modified SnO_2 also exhibited a smoother surface than pristine SnO_2 (Fig. 2(d) and (e)). The root mean square (RMS) of the SnO_2 ETLs was reduced from 5.96 to 4.83 nm according to the AFM measurements (Fig. 2(f) and (g)). The transmittance of ZIF-8 and MACl@ZIF-8-modified SnO_2 slightly increased in comparison to unmodified SnO_2, as revealed by ultraviolet-visible (UV-vis) spectroscopy (Fig. S2, ESI†). We hypothesize that the increased transmittance is due to the even distribution of MACl@ZIF-8, which induces possible optical coupling in the MACl@ZIF-8/SnO_2 layer.[37] In typical planar PSCs, the PCE of the device is directly influenced by the transmittance, which has a close relationship to the number of photogenerated

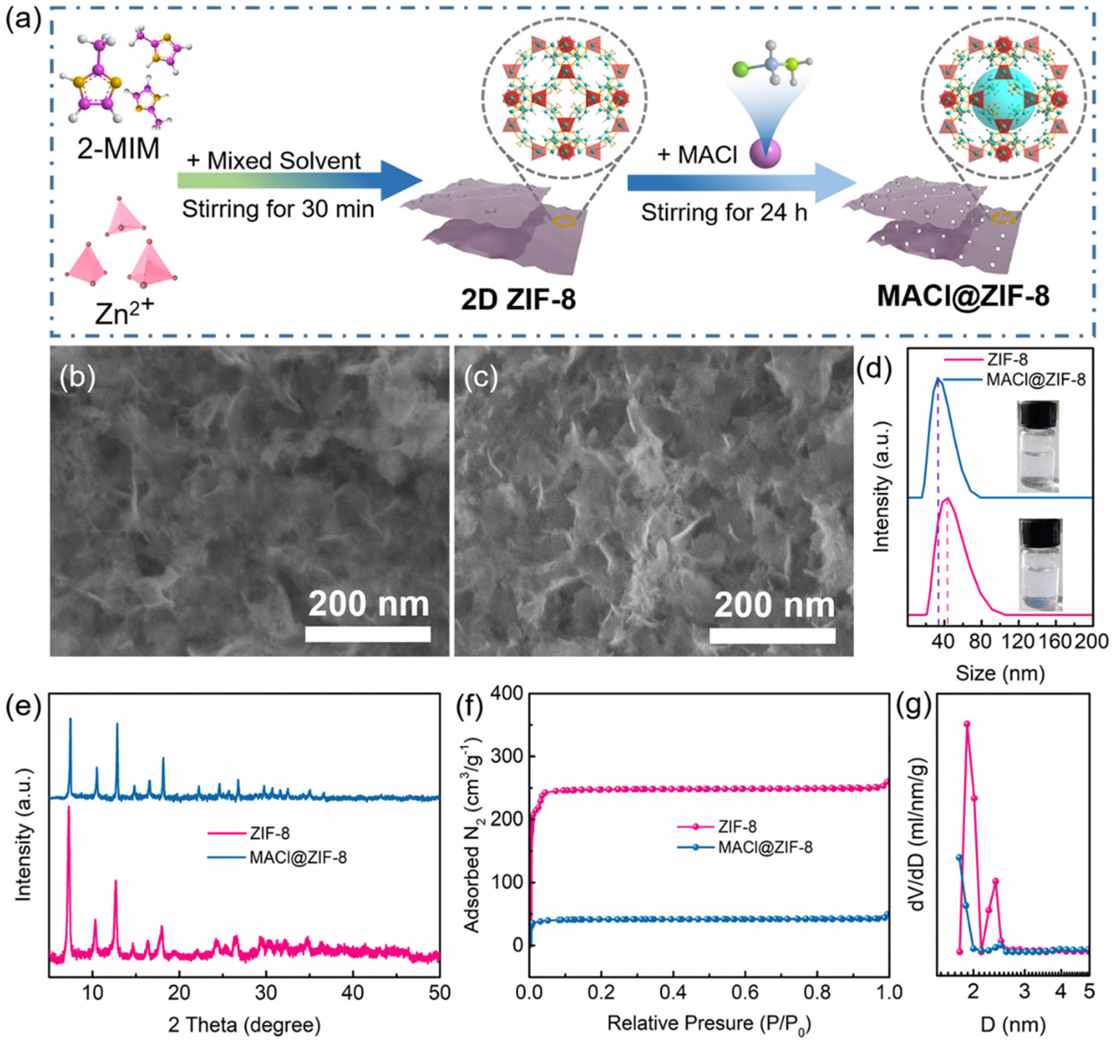

Fig. 1 (a) Illustration of the synthetic process of MACl@ZIF-8. The SEM images of (b) pristine ZIF-8 and (c) MACl@ZIF-8. (d) DLS curves of ZIF-8 and MACl@ZIF-8 dispersants. (e) XRD patterns of ZIF-8 and MACl@ZIF-8. (f) N_2 adsorption/desorption isotherm and (g) pore size distribution.

carriers produced by the active perovskite layer. Additionally, the contact angle of MACl@ZIF-8-modified SnO_2 film is 39.9° (Fig. 2(i)), which is smaller than 49.4° for the pristine SnO_2 (Fig. 2(h)). This change could be attributed to the smoother surface and more hydrophilic sites exposed on ZIF-8. Reasonably, the smaller contact angle would facilitate the spreading of the perovskite precursor solution and the subsequent growth of the crystals.

Fig. 3(a) schematically demonstrates the interaction between SnO_2 and ZIF-8. The presence of uncoordinated N and Zn atoms at the edges of the ZIF-8 framework allows them to passivate the defective sites on the SnO_2 surface[38,39] To verify the speculation, the chemical states were investigated by XPS. As Fig. 3(b) shows, the Sn 3d peaks of MACl@ZIF-8-modified SnO_2 shifted to lower binding energy, while the –NH characteristic peak in the N 1s XPS spectrum was reduced from 45% to 36% (Fig. 3(d)). Therefore, we can infer that the electrons were transferred from the N atoms in MACl@ZIF-8 to the Sn atoms in SnO_2,[40] which indicates that the N atoms in the imidazole of ZIF-8 chemically interacted with the Sn atoms in SnO_2 to form Sn–N bonds.[41] Thus, it is favorable to reduce the number of dangling Sn bonds on the surface of SnO_2. Besides, the O 1s spectra are also divided into two peaks by deconvolution (Fig. 3(c)), where the larger binding energy peak corresponds to the vacancy oxygen and the lower one corresponds to the lattice oxygen of SnO_2. The fraction of oxygen vacancy was reduced from 54% to 38% after MACl@ZIF-8 modification (Table S1, ESI†), indicating that the oxygen vacancies on SnO_2 were effectively passivated.[42] Thus, the MACl@ZIF-8 modification effectively eliminates trap states on SnO_2 and thereby creates fewer barriers for electron transportation.

The energy levels of pristine SnO_2 and MACl@ZIF-8-modified SnO_2 ETLs were investigated by ultraviolet photoemission spectroscopy (UPS). The valence band (E_{VB}), conduction band (E_{CB}), and Fermi level (E_F) were derived from the results of UV-vis and UPS spectra (Fig. S3, ESI†). The E_F of the ETL decreased from 3.82 eV to 3.42 eV, which indicated that the ETL was more n-type and was conducive to electron transfer.[43] Besides, the E_{CB} of MACl@ZIF-8-modified SnO_2 moved up to a higher energy level of

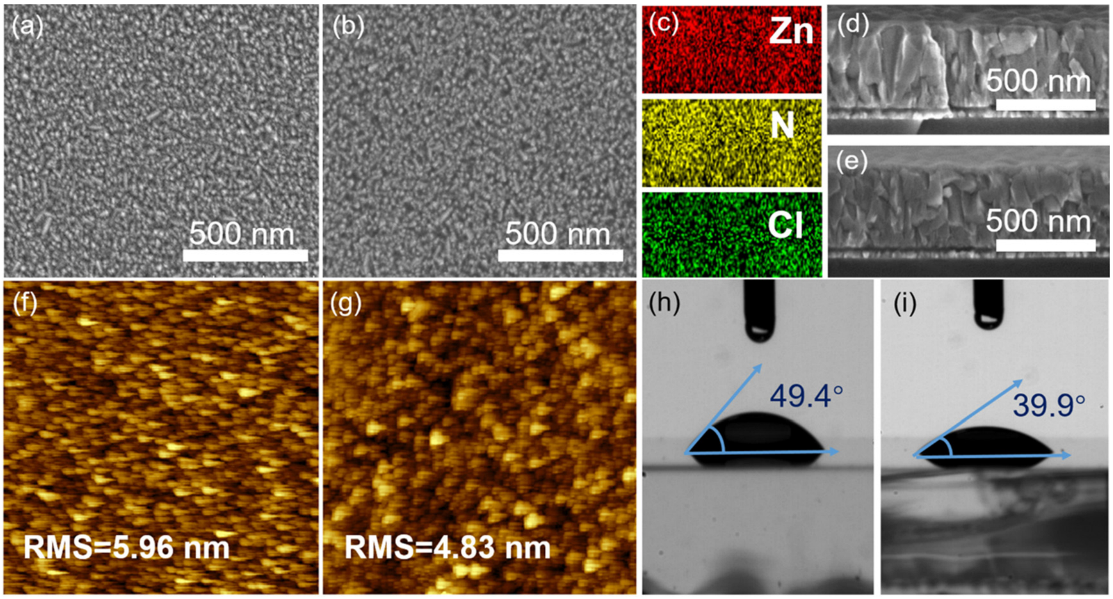

Fig. 2 Top-view and cross-sectional SEM images of (a), (d) SnO_2 and (b), (e) MACl@ZIF-8/SnO_2. (c) EDS mappings of Zn, N, and Cl elements across MACl@ZIF-8/SnO_2. AFM images of (f) SnO_2 and (g) MACl@ZIF-8/SnO_2. The contact angles of (h) SnO_2 and (i) MACl@ZIF-8/SnO_2.

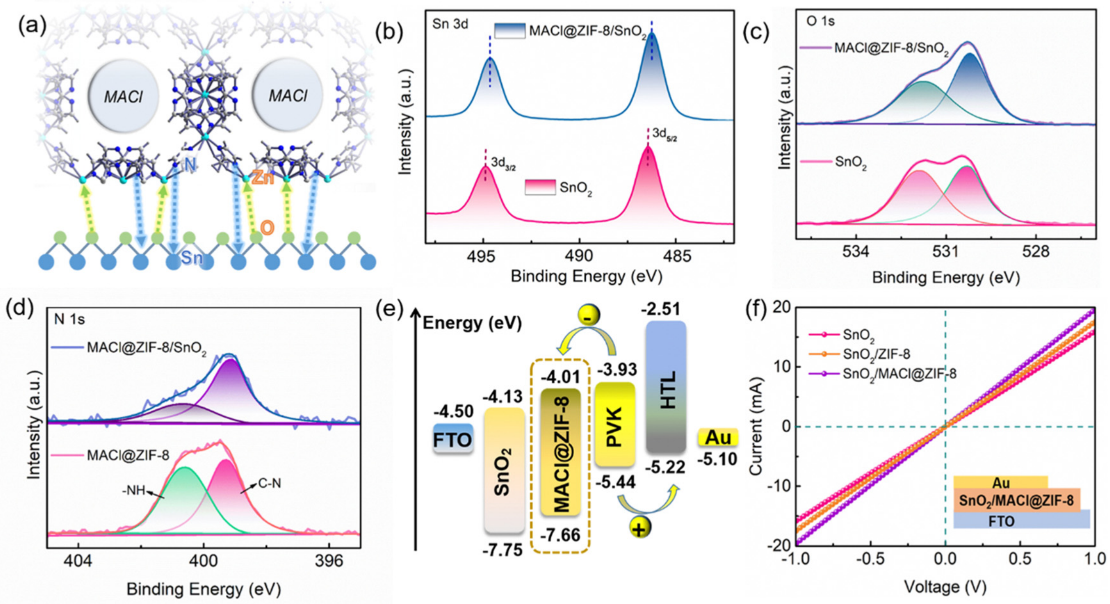

Fig. 3 (a) Schematic diagram of the interaction between ZIF-8 and SnO_2. (b) and (c) Sn 3d and O 1s XPS spectra of SnO_2 and MACl@ZIF-8/SnO_2. (d) N 1s XPS spectra of MACl@ZIF-8 and MACl@ZIF-8/SnO_2. (e) Energy level diagram of the PSCs. (f) Current–voltage curves of the different ETLs sandwiched between Au and FTO.

−4.01 eV, which was closer to the −3.93 eV of the perovskite layer (Fig. 3(e)). Then, the perovskite/SnO_2 interface achieved a favorable energy level alignment which led to less energy loss. Furthermore, the conductivity of MACl@ZIF-8/SnO_2 was calculated from the *I–V* curves under a dark environment (Fig. 3(f)). The equation $\sigma = d/AR$, where d is the thickness of the ETL, R is the resistance, and A is the active area, is used to determine the conductivities (σ) of different ETLs.[44] Consequently, the σ of SnO_2, ZIF-8/SnO_2 and MACl@ZIF-8/SnO_2 are 6.67×10^{-5} S cm^{-1}, 7.54×10^{-5} S cm^{-1} and 8.89×10^{-5} S cm^{-1}, respectively. Hence, MACl@ZIF-8-modified SnO_2 exhibited the best conductivity. From the results of the energy level discussed above, the greater n-type character of MACl@ZIF-8 is conducive to electron transfer and electronic conductivity.[43] Therefore, the extraction and transfer of electrons from the perovskite layer to the ETL showed remarkable improvement.

Here, we adopted the triple-cation mixed perovskite ($(FA_{0.83}MA_{0.17})_{0.95}Cs_{0.05}Pb(I_{0.83}Br_{0.17})_3$) as the light-absorbing

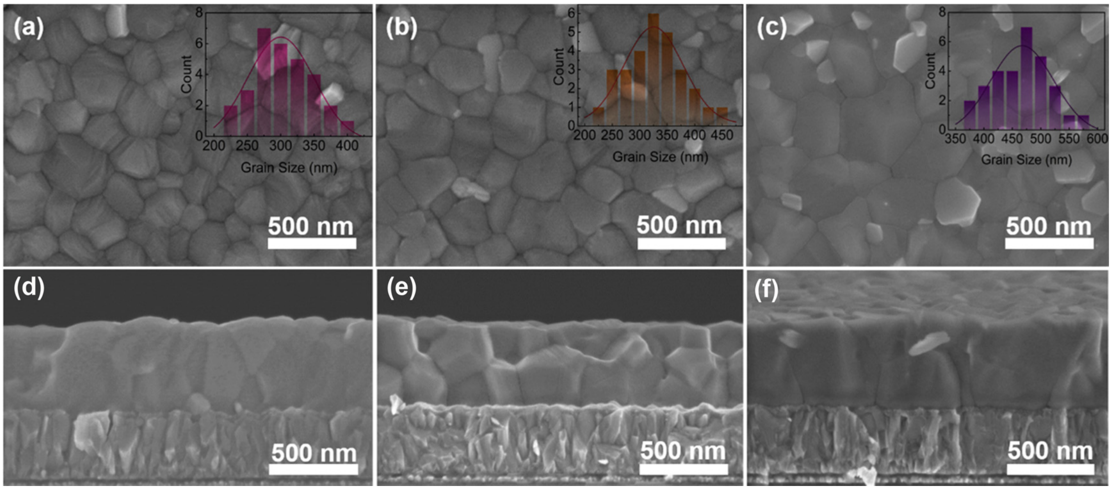

Fig. 4 (a)–(c) Top-view and (d)–(f) cross-sectional SEM images of perovskite films based on SnO_2, ZIF-8/SnO_2 and MACl@ZIF-8/SnO_2, respectively. The insets are grain size distributions.

layer. With the buried interface passivated by 2D MACl@ZIF-8, the perovskite film demonstrated optimized crystallinity and larger grain size than the control sample. As shown in Fig. 4(a)–(c), the perovskite grains on ZIF-8 or MACl@ZIF-8-modified SnO_2 are larger and more compact than that on pristine SnO_2. The corresponding cross-sectional SEM images (Fig. 4(d)–(f)) also clearly demonstrate that the modified perovskite films have better crystallinity, especially for the perovskite based on MACl@ZIF-8/SnO_2, which shows larger grain sizes. The improved crystallinity could be attributed to the following. The surface of the substrate is smoother after 2D MACl@ZIF-8 modification, which is more conducive to the uniform growth of perovskite films with larger grain sizes.[45] (ii) The pre-buried MACl guest in the ZIF-8 host could first react with PbI_2/$PbBr_2$ in the perovskite precursor solution and form perovskite seeds during the spin-coating process, which is conducive to the oriented growth of perovskite crystals.[46] (iii) MACl could form the FAI–MABr–CsI–MACl–PbI_2–$PbBr_2$–DMSO intermediate phase during the solution process, expanding the time window for perovskite crystal growth and thus yielding larger grains;[47] accordingly, the MACl@ZIF-8-modified perovskite films show stronger light absorption (Fig. S4, ESI†). MACl@ZIF-8 modification provides a smoother surface and slightly improves the transmittance of pristine SnO_2. More importantly, MACl@ZIF-8 modification results in high-quality perovskite films with better crystallinity and a purer phase. Thus, the absorption intensity of the perovskite layer based on MACl@ZIF-8-modified SnO_2 is enhanced.

To further verify the crystallinity of the perovskite layer after the buried interface modification, XRD patterns of the perovskite films were obtained (Fig. S5, ESI†). The intensity of the main peak of the perovskite film based on MACl@ZIF-8/SnO_2 was strengthened as compared to that of pristine SnO_2. More importantly, the intensity of the PbI_2 diffraction peak of the ZIF-8 and MACl@ZIF-8-modified perovskite films were greatly reduced as compared to that of the pristine SnO_2. This finding shows that 2D ZIF-8 may significantly suppress the impurity phase in perovskite film by reducing the amount of residual PbI_2 at the buried interface.[46]

Based on the above findings, we investigated the photovoltaic performances of PSCs with and without MACl@ZIF-8 modification. The device had a planar n–i–p heterostructure of FTO/SnO_2/perovskite/Spiro-OMeTAD/Au. As schematically illustrated in Fig. 5(a), MACl@ZIF-8 acts as an interlayer with the effect of multi-passivation. On the one hand, the N and Zn in ZIF-8 could heal the uncoordinated Pb^{2+} and halogen ions at the bottom of the perovskite layer.[48,49] The XPS peak shift of Pb 4f and I 3d in Fig. S6 (ESI†) indicated the interactions. On the other hand, the MA^+ released from ZIF-8 could compensate for the cationic vacancies. The J–V curves of champion devices are shown in Fig. 5(b), the optimal MACl@ZIF-8-modified device achieved an impressive PCE of 22.10% with a high FF of 79.10%, V_{OC} of 1.16 V, and J_{SC} of 24.07 mA cm^{-2}. As a comparison, the control device showed a relatively lower PCE of 19.61% with FF of 77.15%, V_{OC} of 1.10 V, and J_{SC} of 23.52 mA cm^{-2}. Significantly, V_{OC} was obviously enhanced after passivating by MACl@ZIF-8, because MACl@ZIF-8 at the buried interface made good contact between the perovskite layer and the SnO_2 layer, which in turn accelerated electron extraction and led to suppressed carrier recombination. It should also be noted that the Cl^- carried by the 2D modifier could diffuse to the bulk phase of the perovskite during the annealing process, which plays an effective role in regulating perovskite crystallization and passivating the bulk defects.[50,51] To verify the light conversion capability of different devices, the external quantum efficiency (EQE) spectra were obtained. As shown in Fig. S7 (ESI†), the integrated J_{SC} values of the control device, and devices with ZIF-8 and with MACl@ZIF-8 were 23.16, 23.31 and 23.59 mA cm^{-2}, matching well with the J_{SC} values obtained from the J–V curves. The EQE of the ZIF-8 device slightly increased as compared to the control, while the MACl@ZIF-8 device showed the highest EQE values, especially in the 400–600 nm range, resulting in an integrated J_{SC} enhancement. The increased EQE agrees well with the enhanced light absorption mentioned above. Thus, more photogenerated carriers will be generated when the incident

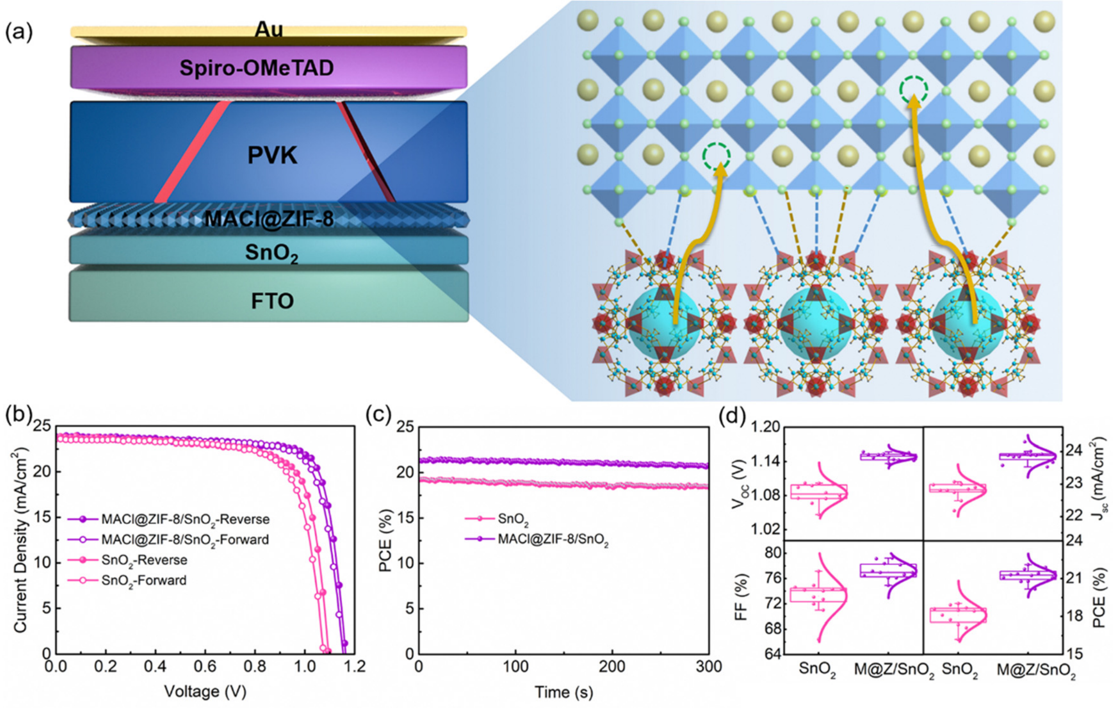

Fig. 5 (a) Schematic illustration of the defect passivation mechanism. (b) Champion *J*–*V* curves of PSCs based on SnO_2 and MACl@ZIF-8-modified SnO_2. (c) Steady PCE out-puts at the MPP. (d) Statistical distributions of device parameters; M@Z is the abbreviation of MACl@ZIF-8.

light is absorbed by the active layer, facilitating the creation of a larger current density.

The steady PCE out-puts at maximum power point (MPP) were measured as shown in Fig. 5(c). With the optimized buried interface and passivated perovskite bulk phase, the PCE of the MACl@ZIF-8 device maintained nearly 21.35%, which is higher as compared to 18.58% for the control device. The statistical distributions of the performance parameters, including V_{OC}, J_{SC}, FF, and PCE, are shown in Fig. 5(d). The average value of each parameter increased and showed excellent reproducibility after the passivation of MACl@ZIF-8.

With the improved device performance, we further determined the mechanism of defect passivation at the buried interface and perovskite phase. Fig. 6(a) shows the dark *J*–*V* curves of devices with and without passivation. The MACl@ZIF-8-modified device exhibited reduced dark current, which

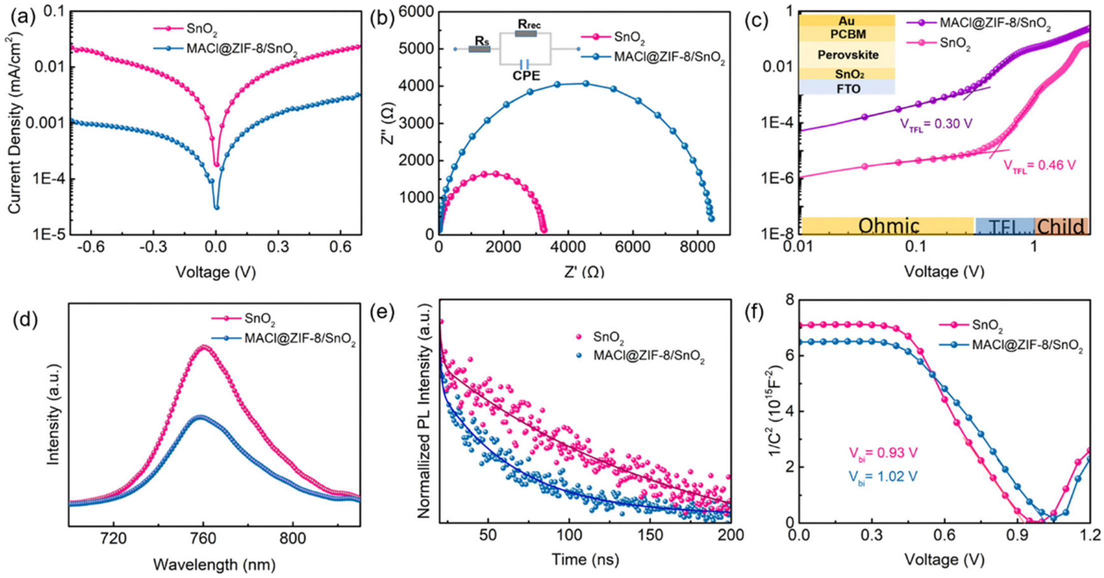

Fig. 6 (a) Dark *J*–*V* curves and (b) Nyquist plots of the PSCs. (c) Dark current–voltage curves of electron-only devices with the structure of FTO/SnO_2/perovskite/PCBM/Au. (d) Steady-state PL and (e) TRPL spectra of perovskite films based on different ETLs. (f) Mott–Schottky plots.

proved that the device has less energy loss during operation.[52] Electrochemical impedance spectroscopy (EIS) was conducted under dark conditions to investigate the charge transfer kinetics within the device. The resultant Nyquist plots are shown in Fig. 6(b), and the series resistance (R_s) and recombination resistance (R_{rec}) were obtained *via* an equivalent circuit model.[53,54] The fitting results showed that the R_{rec} of the MACl@ZIF-8-modified device was 8.5 kΩ, which is larger as compared to 2.5 kΩ of the control device. This demonstrates that the MACl@ZIF-8-modified devices could effectively suppress non-radiative recombination while also being more conducive to charge transfer,[55] which highly matched the results of the dark *J*–*V*. It was further confirmed that the modification of the buried interface by MACl@ZIF-8 accelerated the electron transfer.[4,56] To evaluate the trap density of the perovskite films on different ETLs, we performed space-charge limited current (SCLC) measurements by employing the electron-only structure of FTO/SnO_2/perovskite/PCBM/Ag. Fig. 6(c) shows the current of devices under applied bias voltage in the dark. The trap-state density was calculated *via* the equation $V_{TFL} = eNtd^2/2\varepsilon_0\varepsilon$.[57] From the SCLC curves, it was observed that the V_{TFL} of the device after introducing MACl@ZIF-8 decreased from 0.46 V to 0.30 V, and the calculated trap density of the MACl@ZIF-8-modified device was 5.26×10^{15} cm^{-3}, which is a significantly reduced trap-state density as compared to the control device of 9.31×10^{15} cm^{-3}. This could be attributed to the advantages of dual-passivation of the host–guest system. The non-radiative recombination centers in the perovskite layer and at the buried interface were significantly reduced and faster charge transportation was realized. It is well known that the photovoltage of a solar cell is directly related to its internal luminescence ability.[58] Here, we qualitatively demonstrate the reduction in trap density by recording the difference in luminescence performances of the two devices using a photophysical characterization method.[59] As shown in Fig. S8 (ESI†), the device without MACl@ZIF-8 showed a localized uneven luminescence under applied current and a weak maximum luminescence intensity, while the MACl@ZIF-8-based device showed a uniform and more stable electroluminescence, which suggests that the non-radiative recombination in the modified device is suppressed.

Fig. 6(d) shows the steady-state photoluminescence (PL) spectra. The PL peak intensity of the modified film is lower as compared to that of the control sample, which indicates that the introduction of MACl@ZIF-8 into the buried interface facilitates the reduced number of non-radiative recombination centers as well as higher electron mobility. In general, the uncoordinated defects are regarded as recombination centers and induce severe energy loss at the buried interface. The time-resolved photoluminescence (TRPL) decay measurement was also conducted to investigate the dynamics of photogenerated carriers. Fig. 6(e) shows the fitted results with the bi-exponential decay function. The decay curves are categorized into two decay parts, namely, a fast decay (τ_1) related to the non-radiative recombination at the interface and a slow decay (τ_2) related to the radiative recombination in the perovskite bulk.[60] The main fitted data are shown in Table S2 (ESI†). The average carrier lifetime can be calculated by the following equation:

$$\tau_{ave} = \sum A_i\tau_i^2 \Big/ \sum A_i\tau_i,$$

The average lifetimes of 150 ns and 51 ns were obtained for the control sample and modified perovskite film, demonstrating the strengthened ability of the extraction and transportation of electrons.[61] Furthermore, to study the mechanism of the accelerated electron transportation, the built-in potential (V_{bi}) was determined by Mott–Schottky measurement and the plots are shown in Fig. 6(f). It can be calculated *via* the following equation:

$$1/C^2 = 2(V_{bi} - V)/A^2q\varepsilon\varepsilon_0N_d,$$

where C represents the capacitance of the charge depletion layer, A is the area of the back electrode, q is the elementary charge, N_d is the carrier density, and ε and ε_0 represent the dielectric constant and vacuum dielectric constant, respectively. With the MACl@ZIF-8 modification, the device demonstrated an increased V_{bi} from 0.93 V to 1.02 V and increased N_d from 1.58×10^{16} cm^{-3} to 1.85×10^{16} cm^{-3}, which provided a strengthened charge driving force. Due to the more n-type ETL contributed to the extra built-in field, an enhanced V_{bi} was obtained.[62] The V_{bi} not only facilitates photogenerated carrier separation and collection but also contributes to the V_{OC}.[55] Thus, the increased V_{bi} is also attributed to the enhancement of V_{OC}, which causes less energy loss.[63]

The long-term stability performance was also investigated. In general, ZIF-8 could absorb the photons whose energies were lower than its bandgap due to the low-energy absorption property of the 2-MIM ligand.[64,65] Therefore, the UV absorption characteristic of ZIF-8 prevented the decomposition of the perovskite layer, induced by UV radiation, as illustrated in Fig. 7(a). With the shielding of the MACl@ZIF-8 layer, the perovskite film maintained a high absorption capability after 200 hours of UV irradiation, whereas the perovskite film without MACl@ZIF-8 exhibited severe UV-induced deterioration with an obvious characteristic absorption edge of PbI_2 (Fig. 7(b)). Fig. 7(c) and (e) show the SEM images of perovskite films aged for 100 h without and with the MACl@ZIF-8 layer. There was obvious phase degradation as compared to the passivated sample. To more visually monitor the decomposition process, the perovskite films were stored in air at a relative humidity of around 65%. Fig. 7(d) shows the photographs of the surface morphological changes of the samples. After storage for 800 h, the control perovskite film became completely yellow, while the perovskite film with MACl@ZIF-8 maintained a much slower rate of decomposition. The corresponding XRD patterns of perovskite films aged for 100 h maintained good crystallinity (Fig. 7(f)). In agreement with the photograph, the perovskite film without MACl@ZIF-8 showed a stronger peak of PbI_2. In comparison, the perovskite film with MACl@ZIF-8 passivation exhibited an almost invariable PbI_2 peak, indicating the excellent stability of passivated perovskite film crystals under the attack of moisture. The perovskite films with greater

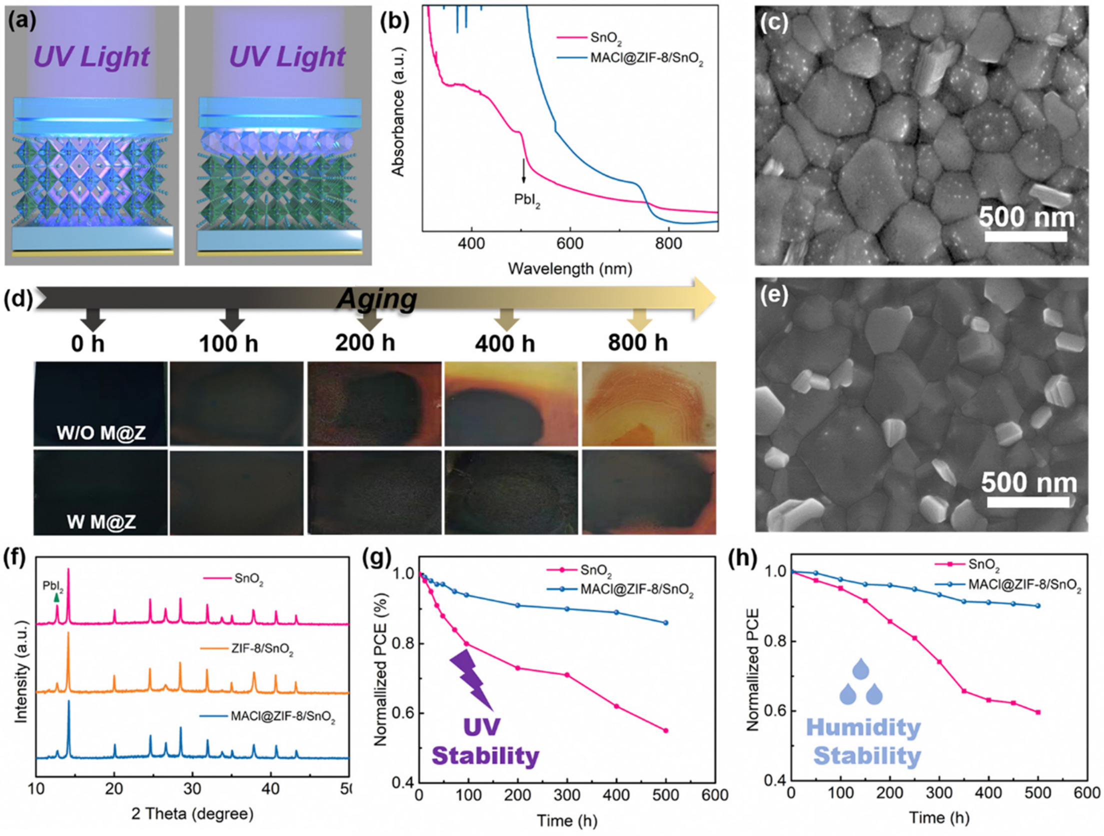

Fig. 7 (a) Schematical illustration of the UV shielding effect of the MACl@ZIF-8 layer. (b) Absorbance spectra of perovskite films after UV irradiation. SEM images of humidity aged (RH = 65%) perovskite films (c) without and (e) with MACl@ZIF-8. (d) Photographs of the perovskite films after aging. (f) XRD patterns of the aged perovskite films. (g) UV stability and (h) humidity stability of devices based on different ETLs without encapsulation.

crystallinity and larger grains are more resistant to moisture and have better long-term stability.[66]

Finally, the photovoltaic performance evolution *versus* time was investigated. As Fig. 7(g) shows, the device with MACl@ZIF-8 can maintain 86% of its original efficiency after 500 hours under UV light exposure. Nevertheless, the efficiency of the control group was below 60% under the same conditions. Moreover, the stability of unencapsulated devices, when exposed to humidity, was tested and the results are shown in Fig. 7(h). The efficiency of the device with MACl@ZIF-8 maintained more than 90% of the original efficiency after 500 h of storage, while the control device only kept less than 60% of its primary efficiency. The enhanced stability can be ascribed to better perovskite crystallinity with a reduced trap state, making the overall device less prone to moisture degradation.[67]

3. Conclusion

We have developed a dual-passivated strategy to reduce the trap density of both the buried interface and perovskite bulk by incorporating a MOF-based host–guest system. Thanks to the robust 2D ZIF-8 and the deep passivation of MACl during the annealing process, the N and Zn in the ZIF-8 host could passivate the uncoordinated Pb^{2+} and I^-/Br^- at the bottom of the perovskite layer, as well as facilitate van der Waals interactions with the SnO_2. Moreover, the MACl guest could provide MA^+ to compensate for cation vacancies in the perovskite layer. Therefore, the MACl@ZIF-8 played a bi-functional passivation role in not only optimizing the buried interfacial contact but also healing the defects of the perovskite bulk phase. As a result, significantly enhanced device performance was obtained and a champion PCE of 22.10% was achieved. Simultaneously, due to the anti-UV characteristic of ZIF-8 and dual-passivation of the host–guest groups, the UV and humidity stability of devices were more prominent than in the pristine devices. Consequently, the MOF-confined MACl in our study provides an innovative perspective and effective method for passivating the buried interface and even other aspects of device defect management.

Conflicts of interest

The authors declare that they have no known competing financial interests or personal relationships that could have appeared to influence the work reported in this paper.

Acknowledgements

This work was supported by the National Natural Science Foundation of China (no. 52202178), Natural Science

Foundation of Shanghai (22ZR1426300), the Shanghai Sailing Program (19YF1417600), and Class III Peak Discipline of Shanghai Materials Science and Engineering (High-Energy Beam Intelligent Processing and Green Manufacturing).

References

1 Best Research-Cell Efficiency Chart. NREL, (**https://www.nrel.gov/pv/cell-efficiency.html**).

2 J. Y. Kim, J. W. Lee, H. S. Jung, H. Shin and N. G. Park, High-Efficiency Perovskite Solar Cells, *Chem. Rev.*, 2020, **120**(15), 7867–7918.

3 Q. Jiang, Y. Zhao, X. W. Zhang, X. L. Yang, Y. Chen, Z. M. Chu, Q. F. Ye, X. X. Li, Z. G. Yin and J. B. You, Surface Passivation of Perovskite Film for Efficient Solar Cells, *Nat. Photonics*, 2019, **13**(7), 460–466.

4 T. P. Li, Y. C. Rui, X. J. Wang, J. S. Shi, Y. Q. Wang, J. X. Yang and Q. H. Zhang, Grain Size and Interface Modification *via* Cesium Carbonate Post-Treatment for Efficient SnO_2-Based Planar Perovskite Solar Cells, *ACS Appl. Energy Mater.*, 2021, **4**(7), 7002–7011.

5 X. J. Wang, Y. Zhao, B. Li, X. F. Han, Z. M. Jin, Y. Q. Wang, Q. H. Zhang and Y. C. Rui, Interfacial Modification *via* a 1,4-Butanediamine-Based 2D Capping Layer for Perovskite Solar Cells with Enhanced Stability and Efficiency, *ACS Appl. Mater. Interfaces*, 2022, **14**(20), 22879–22888.

6 F. Zhang and K. Zhu, Additive Engineering for Efficient and Stable Perovskite Solar Cells, *Adv. Energy Mater.*, 2020, **10**(13), 1902579.

7 L. F. Chao, T. T. Niu, W. Y. Gao, C. X. Ran, L. Song, Y. H. Chen and W. Huang, Solvent Engineering of the Precursor Solution toward Large-Area Production of Perovskite Solar Cells, *Adv. Mater.*, 2021, **33**(14), 2005410.

8 F. Zhang, Y. Z. Hou, S. Wang, H. H. Zhang, F. F. Zhou, Y. Y. Hao, S. Ye, H. Z. Cai, J. Song and J. L. Qu, Solvent-Additive Engineering-Assisted Improvement of Interface Contact for Producing Highly Efficient Inverted Perovskite Solar Cells, *Sol. RRL*, 2021, **5**(7), 2100190.

9 Y. Xu, Y. Rui, X. Wang, B. Li, Z. Jin, Y. Wang and Q. Zhang, Boosted Charge Extraction of SnO_2 Nanorod Arrays *via* Nanostructural and Surface Chemical Engineering for Efficient and Stable Perovskite Solar Cells, *Appl. Surf. Sci.*, 2023, 607, DOI: **10.1016/j.apsusc.2022.154986**.

10 Y. Rui, T. Li, B. Li, Y. Wang and P. Mueller-Buschbaum, Two-Dimensional SnS_2 Nanosheets as Electron Transport and Interfacial Layers Enable Efficient Perovskite Solar Cells, *J. Mater. Chem. C*, 2022, **10**(34), 12392–12401.

11 P. Lv, Y. Yang, N. Li, Y. Zhang, M. Hu, B. Huang, Y. Zhu, Y. Wang, J. Pan, S. Wang, B. Zhang, F. Huang, Y.-B. Cheng and J. Lu, Hypervalent Potassium Xanthate Modified SnO_2 for Highly Efficient Perovskite Solar Modules, *Chem. Eng. J.*, 2023, **456**, 140894.

12 C. Altinkaya, E. Aydin, E. Ugur, F. H. Isikgor, A. S. Subbiah, M. De Bastiani, J. Liu, A. Babayigit, T. G. Allen, F. Laquai, A. Yildiz and S. De Wolf, Tin Oxide Electron-Selective Layers for Efficient, Stable, and Scalable Perovskite Solar Cells, *Adv. Mater.*, 2021, **33**(15), 2005504.

13 X. Yang, D. Luo, Y. Xiang, L. Zhao, M. Anaya, Y. Shen, J. Wu, W. Yang, Y.-H. Chiang, Y. Tu, R. Su, Q. Hu, H. Yu, G. Shao, W. Huang, T. P. Russell, Q. Gong, S. D. Stranks, W. Zhang and R. Zhu, Buried Interfaces in Halide Perovskite Photovoltaics, *Adv. Mater.*, 2021, **33**(7), 2006435.

14 W. Chen, Y. Wang, G. Pang, C. W. Koh, A. B. Djurišić, Y. Wu, B. Tu, F.-Z. Liu, R. Chen, H. Y. Woo, X. Guo and Z. He, Conjugated Polymer–Assisted Grain Boundary Passivation for Efficient Inverted Planar Perovskite Solar Cells, *Adv. Funct. Mater.*, 2019, **29**(27), 1808855.

15 X. Xu, X. Ji, R. Chen, F. Ye, S. Liu, S. Zhang, W. Chen, Y. Wu and W.-H. Zhu, Improving Contact and Passivation of Buried Interface for High-Efficiency and Large-Area Inverted Perovskite Solar Cells, *Adv. Funct. Mater.*, 2022, **32**(9), 2109968.

16 H. Xu, Y. Miao, N. Wei, H. Chen, Z. Qin, X. Liu, X. Wang, Y. Qi, T. Zhang and Y. Zhao, CsI Enhanced Buried Interface for Efficient and UV-Robust Perovskite Solar Cells, *Adv. Energy Mater.*, 2022, **12**(2), 2103151.

17 M. Luo, X. Zong, W. Zhang, M. Hua, Z. Sun, M. Liang and S. Xue, A Multifunctional Fluorinated Polymer Enabling Efficient $MAPbI_3$-Based Inverted Perovskite Solar Cells, *ACS Appl. Mater. Interfaces*, 2022, **14**(27), 31285–31295.

18 J. Cao, X. Lv, P. Zhang, T. T. Chuong, B. Wu, X. Feng, C. Shan, J. Liu and Y. Tang, Plant Sunscreen and Co(II)/(III) Porphyrins for UV-Resistant and Thermally Stable Perovskite Solar Cells: From Natural to Artificial, *Adv. Mater.*, 2018, **30**(27), 1800568.

19 Y. Z. Zhang, Y. J. Wang, L. C. Zhao, X. Y. Yang, C. H. Hou, J. Wu, R. Su, S. Jia, J. J. Shyue, D. Y. Luo, P. Chen, M. T. Yu, Q. Y. Li, L. Li, Q. H. Gong and R. Zhu, Depth-Dependent Defect Manipulation in Perovskites for High-Performance Solar Cells, *Energy Environ. Sci.*, 2021, **14**(12), 6526–6535.

20 H. Zhang, F. T. Eickemeyer, Z. Zhou, M. Mladenović, F. Jahanbakhshi, L. Merten, A. Hinderhofer, M. A. Hope, O. Ouellette, A. Mishra, P. Ahlawat, D. Ren, T.-S. Su, A. Krishna, Z. Wang, Z. Dong, J. Guo, S. M. Zakeeruddin, F. Schreiber, A. Hagfeldt, L. Emsley, U. Rothlisberger, J. V. Milić and M. Grätzel, Multimodal Host–Guest Complexation for Efficient and Stable Perovskite Photovoltaics, *Nat. Commun.*, 2021, **12**(1), 3383.

21 E. Gkaniatsou, C. Sicard, R. Ricoux, L. Benahmed, F. Bourdreux, Q. Zhang, C. Serre, J.-P. Mahy and N. Steunou, Enzyme Encapsulation in Mesoporous Metal–Organic Frameworks for Selective Biodegradation of Harmful Dye Molecules, *Angew. Chem., Int. Ed.*, 2018, **57**(49), 16141–16146.

22 L. Wang, W. Zhi, D. Lian, Y. Wang, J. Han and Y. Wang, HRP@ZIF-8/DNA Hybrids: Functionality Integration of ZIF-8 *via* Biomineralization and Surface Absorption, *ACS Sustainable Chem. Eng.*, 2019, **7**(17), 14611–14620.

23 H.-Y. Li, S.-N. Zhao, S.-Q. Zang and J. Li, Functional Metal-Organic Frameworks as Effective Sensors of Gases and Volatile Compounds, *Chem. Soc. Rev.*, 2020, **49**(17), 6364–6401.

24 S.-L. Hou, J. Dong and B. Zhao, Formation of C-X Bonds in CO_2 Chemical Fixation Catalyzed by Metal−Organic Frameworks, *Adv. Mater.*, 2020, **32**(3), 1806163.

25 M. Li, D. Xia, Y. Yang, X. Du, G. Dong, A. Jiang and R. Fan, Doping of $[In_2(phen)_3Cl_6]\cdot CH_3CN\cdot 2H_2O$ Indium-Based Metal–Organic Framework into Hole Transport Layer for Enhancing Perovskite Solar Cell Efficiencies, *Adv. Energy Mater.*, 2018, **8**(12), 1800552.

26 T.-H. Chang, C.-W. Kung, H.-W. Chen, T.-Y. Huang, S.-Y. Kao, H.-C. Lu, M.-H. Lee, K. M. Boopathi, C.-W. Chu and K.-C. Ho, Planar Heterojunction Perovskite Solar Cells Incorporating Metal–Organic Framework Nanocrystals, *Adv. Mater.*, 2015, **27**(44), 7229–7235.

27 S. Qiu, M. Xue and G. Zhu, Metal–Organic Framework Membranes: from Synthesis to Separation Application, *Chem. Soc. Rev.*, 2014, **43**(16), 6116–6140.

28 Y. Shen, T. Pan, L. Wang, Z. Ren, W. Zhang and F. Huo, Programmable Logic in Metal–Organic Frameworks for Catalysis, *Adv. Mater.*, 2021, **33**(46), 2007442.

29 S. Yuan, L. Feng, K. Wang, J. Pang, M. Bosch, C. Lollar, Y. Sun, J. Qin, X. Yang, P. Zhang, Q. Wang, L. Zou, Y. Zhang, L. Zhang, Y. Fang, J. Li and H.-C. Zhou, Stable Metal–Organic Frameworks: Design, Synthesis, and Applications, *Adv. Mater.*, 2018, **30**(37), 1704303.

30 L. Qiu, K. Xing, J. Zhang, Y. Yang, W. Cao, X. Zhou, K. Zhu, D. Xia and R. Fan, Two-Dimensional Metal–Organic Frameworks-Based Grain Termination Strategy Enables High-Efficiency Perovskite Photovoltaics with Enhanced Moisture and Thermal Stability, *Adv. Funct. Mater.*, 2021, **31**(17), 2010368.

31 J. Ji, B. Liu, H. Huang, X. Wang, L. Yan, S. Qu, X. Liu, H. Jiang, M. Duan, Y. Li and M. Li, Nondestructive Passivation of The TiO_2 Electron Transport Layer in Perovskite Solar Cells by The PEIE-2D MOF Interfacial Modified Layer, *J. Mater. Chem. C*, 2021, **9**(22), 7057–7064.

32 S. F. Wu, Z. Li, M. Q. Li, Y. X. Diao, F. Lin, T. T. Liu, J. Zhang, P. Tieu, W. P. Gao, F. Qi, X. Q. Pan, Z. T. Xu, Z. L. Zhu and A. K. Y. Jen, 2D Metal–Organic Framework for Stable Perovskite Solar Cells with Minimized Lead Leakage, *Nat. Nanotechnol.*, 2020, **15**(11), 934–940.

33 N. Liédana, A. Galve, C. Rubio, C. Téllez and J. Coronas, CAF@ZIF-8: One-Step Encapsulation of Caffeine in MOF, *ACS Appl. Mater. Interfaces*, 2012, **4**(9), 5016–5021.

34 X. Jiang, S. He, G. Han, J. Long, S. Li, C. H. Lau, S. Zhang and L. Shao, Aqueous One-Step Modulation for Synthesizing Monodispersed ZIF-8 Nanocrystals for Mixed-Matrix Membrane, *ACS Appl. Mater. Interfaces*, 2021, **13**(9), 11296–11305.

35 C.-P. Li and M. Du, Role of Solvents in Coordination Supramolecular Systems, *Chem. Commun.*, 2011, **47**(21), 5958–5972.

36 B. Li, Y. Rui, J. Xu, Y. Wang, J. Yang, Q. Zhang and P. Mueller-Buschbaum, Solution-Processed p-Type Nanocrystalline CoO Films for Inverted Mixed Perovskite Solar Cells, *J. Colloid Interface Sci.*, 2020, **573**, 78–86.

37 X. Yang, L. Li, J. Wu, Q. Hu, Y. Wang, T. P. Russell, Y. Tu and R. Zhu, Optimizing Vertical Crystallization for Efficient Perovskite Solar Cells by Buried Composite Layers, *Sol. RRL*, 2021, **5**(10), 2100457.

38 M. Zhan, C. Ge, S. Hussain, A. S. Alkorbi, R. Alsaiari, N. A. Alhemiary, G. Qiao and G. Liu, Enhanced NO_2 Gas-Sensing Performance by Core-Shell SnO_2/ZIF-8 Nanospheres, *Chemosphere*, 2022, **291**, 132842.

39 P. G. Choi, Z. Liu, N. Hara and Y. Masuda, Surface Molecular Separator for Selective Gas Sensing, *Ind. Eng. Chem. Res.*, 2020, **59**(40), 17894–17900.

40 M. E. Dmello, N. G. Sundaram and S. B. Kalidindi, Assembly of ZIF-67 Metal–Organic Framework over Tin Oxide Nanoparticles for Synergistic Chemiresistive CO_2 Gas Sensing, *Chem. – Eur. J.*, 2018, **24**(37), 9220–9223.

41 M. E. Dmello, N. G. Sundaram and S. B. Kalidindi, Assembly of ZIF-67 Metal-Organic Framework over Tin Oxide Nanoparticles for Synergistic Chemiresistive CO_2 Gas Sensing, *Chem. – Eur. J.*, 2018, **24**(37), 9220–9223.

42 Y. Xu, Y. Rui, X. Wang, B. Li, Z. Jin, Y. Wang, W. An and Q. Zhang, Dual Passivation of SnO_2/Perovskite Heterogeneous Interfacial Defects for Efficient Perovskite Solar Cells, *Sol. Energy Mater. Sol. Cells*, 2023, **250**, 112088.

43 W. Wu, W. Han, Y. Deng, G. Ren, C. Liu and W. Guo, Low-Cost and Easily Prepared Interface Layer Towards Efficient and Negligible Hysteresis Perovskite Solar Cells, *J. Colloid Interface Sci.*, 2022, **617**, 745–751.

44 T. Li, Y. Rui, X. Zhang, J. Shi, X. Wang, Y. Wang, J. Yang and Q. Zhang, Anatase TiO_2 Nanorod Arrays as High-Performance Electron Transport Layers for Perovskite Solar Cells, *J. Alloys Compd.*, 2020, **849**, 156629.

45 D. Shen, A. Pang, Y. Li, J. Dou and M. Wei, Metal–Organic Frameworks at Interfaces of Hybrid Perovskite Solar Cells for Enhanced Photovoltaic Properties, *Chem. Commun.*, 2018, **54**(10), 1253–1256.

46 Z. Hu, Q. An, H. Xiang, L. Aigouy, B. Sun, Y. Vaynzof and Z. Chen, Enhancing the Efficiency and Stability of Triple-Cation Perovskite Solar Cells by Eliminating Excess PbI_2 from the Perovskite/Hole Transport Layer Interface, *ACS Appl. Mater. Interfaces*, 2020, **12**(49), 54824–54832.

47 M. Mateen, Z. Arain, Y. Yang, X. Liu, S. Ma, C. Liu, Y. Ding, X. Ding, M. Cai and S. Dai, MACl-Induced Intermediate Engineering for High-Performance Mixed-Cation Perovskite Solar Cells, *ACS Appl. Mater. Interfaces*, 2020, **12**(9), 10535–10543.

48 R. Chen, D. Hou, C. Lu, J. Zhang, P. Liu, H. Tian, Z. Zeng, Q. Xiong, Z. Hu, Y. Zhu and L. Han, Zinc Ion as Effective Film Morphology Controller in Perovskite Solar Cells, *Sustainable Energy Fuels*, 2018, **2**(5), 1093–1100.

49 S. Yu, J. Meng, Q. Pan, Q. Zhao, T. Pullerits, Y. Yang, K. Zheng and Z. Liang, Imidazole Additives in 2D Halide Perovskites: Impacts of $-CN$ *versus* $-CH_3$ Substituents Reveal the Mediation of Crystal Growth by Phase Buffering, *Energy Environ. Sci.*, 2022, **15**(8), 3321–3330.

50 H. R. Tan, A. Jain, O. Voznyy, X. Z. Lan, F. P. G. de Arquer, J. Z. Fan, R. Quintero-Bermudez, M. J. Yuan, B. Zhang, Y. C. Zhao, F. J. Fan, P. C. Li, L. N. Quan, Y. B. Zhao, Z. H. Lu, Z. Y. Yang, S. Hoogland and E. H. Sargent, Efficient

and Stable Solution-Processed Planar Perovskite Solar Cells *via* Contact Passivation, *Science*, 2017, **355**(6326), 722–726.

51 Z. Li, L. Wang, R. Liu, Y. Fan, H. Meng, Z. Shao, G. Cui and S. Pang, Spontaneous Interface Ion Exchange: Passivating Surface Defects of Perovskite Solar Cells with Enhanced Photovoltage, *Adv. Energy Mater.*, 2019, **9**(38), 1902142.

52 W. Zhao, H. Lin, Y. Li, D. Wang, J. Wang, Z. Liu, N. Yuan, J. Ding, Q. Wang and S. Liu, Symmetrical Acceptor–Donor–Acceptor Molecule as a Versatile Defect Passivation Agent toward Efficient $FA_{0.85}MA_{0.15}PbI_3$ Perovskite Solar Cells, *Adv. Funct. Mater.*, 2022, **32**(19), 2112032.

53 X. Fan, Y. Rui, X. Han, J. Yang, Y. Wang and Q. Zhang, Spray-Coated Monodispersed SnO_2 Microsphere Films as Scaffold Layers for Efficient Mesoscopic Perovskite Solar Cells, *J. Power Sources*, 2020, **448**, 227405.

54 Y. Rui, Z. Jin, X. Fan, W. Li, B. Li, T. Li, Y. Wang, L. Wang and J. Liang, Defect Passivation and Electrical Conductivity Enhancement in Perovskite Solar Cells Using Functionalized Graphene Quantum Dots, *Mater. Futures*, 2022, **1**(4), 045101.

55 H. Ma, M. Wang, Y. Wang, Q. Dong, J. Liu, Y. Yin, J. Zhang, M. Pei, L. Zhang, W. Cai, L. Shi, W. Tian, S. Jin, J. Bian and Y. Shi, Asymmetric Organic Diammonium Salt Buried in SnO_2 Layer Enables Fast Carrier Transfer and Interfacial Defects Passivation for Efficient Perovskite Solar Cells, *Chem. Eng. J.*, 2022, **442**, 136291.

56 J. Lee, N. Tsvetkov, S. R. Shin and J. K. Kang, Fast Charge Transfer and High Stability *via* Hybridization of Hygroscopic Cu-BTC Metal–Organic Framework Nanocrystals with a Light-Absorbing Layer for Perovskite Solar Cells, *ACS Appl. Mater. Interfaces*, 2022, **14**(31), 35495–35503.

57 Z. Zhu, Y. Bai, X. Liu, C.-C. Chueh, S. Yang and A. K. Y. Jen, Enhanced Efficiency and Stability of Inverted Perovskite Solar Cells Using Highly Crystalline SnO_2 Nanocrystals as the Robust Electron-Transporting Layer, *Adv. Mater.*, 2016, **28**(30), 6478–6484.

58 Y. Fan, H. Chen, X. Liu, M. Ren, Y. Liang, Y. Wang, Y. Miao, Y. Chen and Y. Zhao, Myth behind Metastable and Stable n-Hexylammonium Bromide-Based Low-Dimensional Perovskites, *J. Am. Chem. Soc.*, 2023, **145**(14), 8209–8217.

59 M. Kim, J. Jeong, H. Lu, T. K. Lee, F. T. Eickemeyer, Y. Liu, I. W. Choi, S. J. Choi, Y. Jo, H.-B. Kim, S.-I. Mo, Y.-K. Kim, H. Lee, N. G. An, S. Cho, W. R. Tress, S. M. Zakeeruddin, A. Hagfeldt, J. Y. Kim, M. Grätzel and D. S. Kim, Conformal Quantum Dot–SnO_2 Layers as Electron Transporters for Efficient Perovskite Solar Cells, *Science*, 2022, **375**(6578), 302–306.

60 Y. Deng, Q. Dong, C. Bi, Y. Yuan and J. Huang, Air-Stable, Efficient Mixed-Cation Perovskite Solar Cells with Cu Electrode by Scalable Fabrication of Active Layer, *Adv. Energy Mater.*, 2016, **6**(11), 1600372.

61 X. Zhang, Y. Rui, Y. Wang, J. Xu, H. Wang, Q. Zhang and P. Mueller-Buschbaum, SnO_2 Nanorod Arrays with Tailored Area Density as Efficient Electron Transport Layers for Perovskite Solar Cells, *J. Power Sources*, 2018, **402**, 460–467.

62 L. Wang, J. Xia, Z. Yan, P. Song, C. Zhen, X. Jiang, G. Shao, Z. Qiu, Z. Wei, J. Qiu and M. K. Nazeeruddin, Robust Interfacial Modifier for Efficient Perovskite Solar Cells: Reconstruction of Energy Alignment at Buried Interface by Self-Diffusion of Dopants, *Adv. Funct. Mater.*, 2022, **32**(35), 2204725.

63 K. Emshadi, N. Ghimire, A. Gurung, B. Bahrami, R. Pathak, R. S. Bobba, B. S. Lamsal, S. I. Rahman, A. H. Chowdhury, K. Chen, M. A. R. Laskar, W. Luo, H. Elbohy and Q. Qiao, Tailoring the Grain Boundaries of Wide-Bandgap Perovskite Solar Cells by Molecular Engineering, *Sol. RRL*, 2020, **4**(12), 2000384.

64 X. Yang and D. Yan, Direct White-Light-Emitting and Near-Infrared Phosphorescence of Zeolitic Imidazolate Framework-8, *Chem. Commun.*, 2017, **53**(11), 1801–1804.

65 T. Du, H. Jiang and X. Wang, Understanding the Photochemical Response of Zeolitic Imidazolate Framework-8 in the Sight of Framework, Uncoordinated 2-Methylimidazole and ZnxOy Clusters. The, *J. Phys. Chem. C*, 2017, **121**(22), 12278–12284.

66 Y. Dong, W. Shen, W. Dong, C. Bai, J. Zhao, Y. Zhou, F. Huang, Y.-B. Cheng and J. Zhong, Chlorobenzenesulfonic Potassium Salts as the Efficient Multifunctional Passivator for the Buried Interface in Regular Perovskite Solar Cells, *Adv. Energy Mater.*, 2022, **12**(20), 2200417.

67 J. Li, L. Zuo, H. Wu, B. Niu, S. Shan, G. Wu and H. Chen, Universal Bottom Contact Modification with Diverse 2D Spacers for High-Performance Inverted Perovskite Solar Cells, *Adv. Funct. Mater.*, 2021, **31**(35), 2104036.